MOX-Report No. 63/2015

Large Eddy Simulations for blood fluid-dynamics in real stenotic carotids

Lancellotti, R.M.; Vergara, C.; Valdettaro, L.; Bose, S.;

Quarteroni, A.

MOX, Dipartimento di Matematica
Politecnico di Milano, Via Bonardi 9 - 20133 Milano (Italy)

mox-dmat@polimi.it http://mox.polimi.it

Large Eddy Simulations for blood fluid-dynamics in real stenotic carotids

Rocco M. Lancellotti[1], Christian Vergara[1], Lorenzo Valdettaro[1], Sanjeeb Bose[2], Alfio Quarteroni[3]

December 3, 2015

[1] MOX, Dipartimento di Matematica, Politecnico di Milano, Italy, {roccomichele.lancellotti,christian.vergara,lorenzo.valdettaro}@polimi.it
[2] Institute for Computational and Mathematical Engineering (ICME), Stanford University, Stanford (CA), USA stbose@stanford.edu
[3] Chair of Modelling and Scientific Computing, École Polytechnique Fédérale de Lausanne, Switzerland, alfio.quarteroni@epfl.ch

Keywords: Large Eddy Simulations, stenotic carotids, shear layer

Abstract

In this paper, we consider Large Eddy Simulations (LES) for human stenotic carotids in presence of atheromasic plaque. It is well known that in such a pathological condition, transitional effects to turbulence may occur, with relevant clinical implications such as plaque rupture. The first aim of this work is to provide a way to define a Direct Numerical Simulation (DNS). In our context turbulence is not statistically homogeneous isotropic and stationary. We define mesh size and time step by considering the reduced model of a 2D shear layer. Then, we compare the performance of LES σ model (both static and dynamic) and of mixed LES models (where also a similarity model is considered) with that of DNS in a realistic scenario of a carotid. The results highlight the effectiveness of the LES σ models in terms of accuracy, especially for the static model.

1 Introduction

The carotid bifurcation is a preferential site of atheromasic plaque formation, which leads to vessel stenosis and, possibly, to the plaque breakage with embolization of fragments into the brain tissue [47, 55]. The blood fluid-dynamics has been recognized to play a crucial role in the plaque rupture, due to the high wall shear stresses (WSS) and high pressure exerted at the stenosis [40, 20, 25].

The percentage of stenosis could rise up to 75-80% of the lumen (or even higher). Several laboratory experiments highlighted that the blood fluid-dynamics in such conditions may undergo transition to *turbulence* [7, 11, 2, 22]. In particular, during the systolic and deceleration phases, a fluid jet with two long shear layers at its sides is created. The shear layers could become unstable and the jet consequently breaks down with formation of recirculation zones and vortices. The presence of transitional effects seems to have a role in the plaque rupture, because large spatial WSS, high temporal shear gradients, and pressure fluctuations, which are known to weaken the plaque, increase with turbulence, [13, 32, 29].

For all these reasons, computational models used to study the fluid-dynamics in stenotic carotids should ideally be able to resolve the Kolmogorov scale (e.g. the smallest dynamically important flow structure), according to the so-called Direct Numerical Simulation (DNS), or provide a turbulence closure to model unresolved eddies. In fact, this was the case of several studies in the recent years; among those that considered real scenarios, we mention [43, 5, 44, 19] for *RANS* models, and [23] for DNS simulations. Recently, *Large Eddy Simulations* (LES) have also been considered in this context, see, e.g., [16, 45, 33, 30]. LES models are based on introducing a filtering procedure that separates the *resolved scales* from the *subgrid scales*, the latter being suitably modelled as a function of the resolved quantities [41, 37, 9].

All the aforementioned works related to the use of LES models for stenotic carotids considered idealized geometries. The results reported therein laid the foundations for the use of LES models in geometries of clinical relevance. However, it is known that although the Reynolds number is not very large (1500-2500), the shape of the stenotic carotid bifurcation together with the pulsatility of the forcing term could promote the development of transition to turbulence for Reynolds numbers less than 2000 (the critical value holding for a pipe) [42]. Thus, DNS could be prohibitive due to the requested computational effort and a comprehensive study of the suitability of LES models in the context of stenotic carotids should consider real scenarios, that is *patient-specific* geometries and boundary data.

In the present work, we compared the results obtained by using different LES models in a real context of a stenotic carotid. At the best of the authors' knowledge, this is the first time that LES models have been applied to a patient-specific carotid artery. To make the comparison complete, we also considered the solution obtained by using a DNS. In all the cases, a SUPG technique has been used to stabilize our numerical schemes due to the presence of high convective terms (high Reynolds numbers).

The outline of the paper is as follows. In Section 2 we introduce the mathematical setting, whereas in Section 3 we report the numerical discretization. In Section 4, we first give a brief discussion on the choice of the time and space discretization parameters, and then we show several numerical results and related comments. Finally, in Section 5 we draw some conclusions.

2 Mathematical models

2.1 The fluid equations

Blood in medium and large vessels could be modelled as an incompressible and homogeneous fluid [15]. Although some works highlighted that in idealized stenotic channels with squared cross-section the shear layer is more elongated when non-Newtonian models are used [43, 30], we decided here to use a Newtonian model, because no evidence of the influence of blood rheology were observed so far for stenotic pipes and real geometries. Moreover, we remark that the LES models we tested have been proposed in the framework of the Newtonian hypothesis. We therefore consider the following Navier-Stokes equations (normalized over the fluid density):

Find the velocity $\boldsymbol{u}(t,\boldsymbol{x})$ and the pressure $p(t,\boldsymbol{x})$ such that

$$\begin{array}{ll} \dfrac{\partial \boldsymbol{u}}{\partial t} - \nu\nabla\cdot\boldsymbol{S}(\boldsymbol{u}) + \nabla\cdot(\boldsymbol{u}\otimes\boldsymbol{u}) + \nabla p = \boldsymbol{0} & t\in(0,T],\ \boldsymbol{x}\in\Omega\subset\mathbb{R}^3, \\ \nabla\cdot\boldsymbol{u} = 0 & t\in(0,T],\ \boldsymbol{x}\in\Omega, \\ \boldsymbol{u} = \boldsymbol{g} & t\in(0,T],\ \boldsymbol{x}\in\Gamma_D, \\ -p\boldsymbol{n} + \nu\boldsymbol{S}(\boldsymbol{u})\boldsymbol{n} = \boldsymbol{\psi} & t\in(0,T],\ \boldsymbol{x}\in\Gamma_N, \end{array} \tag{1}$$

with a quiescent initial boundary condition, and where $(\boldsymbol{u}\otimes\boldsymbol{u})_{ij} = u_i u_j$, $\boldsymbol{S}(\boldsymbol{u}) = \nabla\boldsymbol{u} + (\nabla\boldsymbol{u})^T$, $\Gamma_D\cup\Gamma_N = \partial\Omega$, $\Gamma_D\cap\Gamma_N = \emptyset$, ν is the kinematic viscosity, and $\boldsymbol{g}(t,\boldsymbol{x})$ and $\boldsymbol{\psi}(t,\boldsymbol{x})$ are given boundary data.

LES models are based on the decomposition of the fluid unknowns in resolved and unresolved quantities, $[\overline{\boldsymbol{u}},\overline{p}]$ and $[\boldsymbol{u}',p']$, respectively, so that $\boldsymbol{u} = \overline{\boldsymbol{u}}+\boldsymbol{u}'$ and $p = \overline{p}+p'$ [37]. The resolved quantities are often referred to as *filtered*, since the following filtering operation is considered:

$$\overline{\boldsymbol{u}}(\boldsymbol{x}) = \int_\Omega \boldsymbol{u}(\boldsymbol{x}')\overline{G}(\boldsymbol{x},\boldsymbol{x}';\overline{\Delta})d\boldsymbol{x}'$$

where $\overline{G}$ is the filter function and $\overline{\Delta}$ is the filter width. The previous operation is formal since $\boldsymbol{u}$ is not known. In order to derive a set of equations for $\overline{\boldsymbol{u}}$ and $\overline{p}$, a filtering procedure is performed over the Navier-Stokes equations (1). Defining

$$\boldsymbol{\tau} = \overline{\boldsymbol{u}\otimes\boldsymbol{u}} - \overline{\boldsymbol{u}}\otimes\overline{\boldsymbol{u}}, \tag{2}$$

we obtain the following fluid momentum equation in the filtered unknowns

$$\frac{\partial\overline{\boldsymbol{u}}}{\partial t} - \nu\nabla\cdot\boldsymbol{S}(\overline{\boldsymbol{u}}) + \nabla\cdot(\overline{\boldsymbol{u}}\otimes\overline{\boldsymbol{u}}) + \nabla\overline{p} + \nabla\cdot\boldsymbol{\tau} = \boldsymbol{0} \quad t\in(0,T],\ \boldsymbol{x}\in\Omega. \tag{3}$$

The tensor $\boldsymbol{\tau}$ is the so called *subgrid-scale* term, which models the effect of the smallest (unresolved) scales on the resolved ones [41, 36]. Different choices for the subgrid-scale tensor lead to different LES models. In any case, $\boldsymbol{\tau}$ is built as a

function of the filtered quantities $\overline{\boldsymbol{u}}$, hence equation (3) only depends on $(\overline{\boldsymbol{u}}, \overline{p})$. A general strategy consists in modeling the deviatoric part $\boldsymbol{\tau}^d = \boldsymbol{\tau} - \frac{1}{3}\sum_k \tau_{kk}\boldsymbol{I}$ of $\boldsymbol{\tau}$, and to define the (unknown) modified filtered pressure $\overline{P} = \overline{p} + \frac{1}{3}\sum_k \tau_{kk}$. Then, the filtered Navier-Stokes equations reads

Find the filtered velocity $\overline{\boldsymbol{u}}$ and pressure $\overline{P}$ such that

$$\begin{aligned}
&\frac{\partial \overline{\boldsymbol{u}}}{\partial t} - \nu\nabla\cdot\boldsymbol{S}(\overline{\boldsymbol{u}}) + \nabla\cdot(\overline{\boldsymbol{u}}\otimes\overline{\boldsymbol{u}}) + \nabla\overline{P} + \nabla\cdot\boldsymbol{\tau}^d(\overline{\boldsymbol{u}}) = \boldsymbol{0} && t\in(0,T],\ \boldsymbol{x}\in\Omega,\\
&\nabla\cdot\overline{\boldsymbol{u}} = 0 && t\in(0,T],\ \boldsymbol{x}\in\Omega,\\
&\overline{\boldsymbol{u}} = \boldsymbol{g} && t\in(0,T],\ \boldsymbol{x}\in\Gamma_D,\\
&-\overline{P}\boldsymbol{n} + \nu\boldsymbol{S}(\overline{\boldsymbol{u}})\boldsymbol{n} - \boldsymbol{\tau}^d(\overline{\boldsymbol{u}})\boldsymbol{n} = \boldsymbol{\psi} && t\in(0,T],\ \boldsymbol{x}\in\Gamma_N,
\end{aligned} \tag{4}$$

with the same initial condition of the unfiltered problem (1). A special remark should be highlighted for what concerns boundary conditions. Indeed, often LES models are written for unbounded domains, thus, in practice, with periodic boundary conditions. Here, we have assumed that the boundary conditions in the filtered equations (4) are the same of the unfiltered problem (1), since both problems want to describe the same physical phenomenon. In particular, we have here proposed to use at the left hand side of the Neumann condition $(4)_4$ the total stress tensor (thus including also the subgrid stress tensor $\boldsymbol{\tau}^d$). This is consistent with the observation that the Neumann condition is a "natural" condition representing what remains from integration by parts when the weak formulation is considered (see Section 3.2).

2.2 Eddy viscosity and hybrid models

Usually, the effect of the subgrid-scale motions on the resolved scales is modeled in analogy with the kinetic theory of gases, by introducing a subgrid-scale viscosity ν_{sgs} and by modeling the deviatoric part of $\boldsymbol{\tau}$ as follows

$$\boldsymbol{\tau}^d(\overline{\boldsymbol{u}}) = -2\nu_{sgs}(\overline{\boldsymbol{u}})\boldsymbol{S}(\overline{\boldsymbol{u}}), \tag{5}$$

where we have highlighted the general dependence of ν_{sgs} on the filtered velocity, depending on the model considered. The models based on (5) produce the mean (in the statistical sense) dissipation provided by the unresolved eddies. In particular, in this work we considered two eddy viscosity models. The first one is the classical Smagorinsky model [41] based on the following choice

$$\nu_{sgs} = \nu_{sgs}^{Smag}(\boldsymbol{x}) = C\overline{\Delta}^2\sqrt{2\sum_{i,j}\overline{S}_{ij}},$$

where we have set $\overline{\boldsymbol{S}} = \boldsymbol{S}(\overline{\boldsymbol{u}})$, $\overline{\Delta}$ is the characteristic length of the filter and C a constant to be suitably chosen. The Smagorinky model has the nice feature to vanish for pure rotations; however it does not vanish in near-wall regions and

for pure shear [31]. Another limitation of this model is that it is too dissipative in laminar regions [18]. It has been used in several works for the analysis of the fluid-dynamics in stenotic (although ideal) vessels, see [16, 45, 33, 30].

The second eddy viscosity model considered in this work is the σ model, introduced in [31]. This model is based on the introduction of the singular values $\sigma_1(t,\boldsymbol{x}) \geq \sigma_2(t,\boldsymbol{x}) \geq \sigma_3(t,\boldsymbol{x}) > 0$ of $\nabla\overline{\boldsymbol{u}}$, and on the following choice

$$\nu_{sgs} = \nu_{sgs}^{\sigma}(t,\boldsymbol{x}) = C\overline{\Delta}^2 \frac{\sigma_3(\sigma_1-\sigma_2)(\sigma_2-\sigma_3)}{\sigma_1^2}, \tag{6}$$

where again C is a constant to be suitably chosen. The σ model vanishes in the cases of pure rotation (like the Smagorisnky model), pure shear, and when the resolved scales are in axisymmetric or isotropic expansion. Moreover, the turbulent stresses decay as the distance to the solid boundary to the third power. In the context of hemodynamics, the σ model has been successfully applied to describe the ventricular blood fluid-dynamics [10].

A new family of LES models has been introduced starting from the eddy viscosity models. These are the so called *mixed* models, where it is assumed to know the expression of a part of $\boldsymbol{\tau}^d$, which does not need to be modeled. The latter is obtained from the *similarity* model by Bardina [3, 28], which, in constrast with the eddy viscosity models, is able to represent the backscatter of energy from subgrid to resolved scales, and is given by the deviatoric part $\boldsymbol{\mathcal{L}}^d$ of

$$\boldsymbol{\mathcal{L}} = \overline{\overline{\boldsymbol{u}}\otimes\overline{\boldsymbol{u}}} - \overline{\overline{\boldsymbol{u}}}\otimes\overline{\overline{\boldsymbol{u}}}. \tag{7}$$

The previous tensor is obtained by considering a filtering of the filtered quantities. Bardina proposed to use the previous quantity to model the whole subgrid-scale tensor $\boldsymbol{\tau}$. In [56, 53, 38] a dissipation term is added as in the eddy viscosity models. This leads to mixed models with

$$\boldsymbol{\tau}^d(\overline{\boldsymbol{u}}) = \boldsymbol{\mathcal{L}}^d(\overline{\boldsymbol{u}}) - 2\nu_{sgs}(\overline{\boldsymbol{u}})\boldsymbol{S}(\overline{\boldsymbol{u}}).$$

In the previous expression, one could consider either the Smagorinsky or the σ model (or another eddy viscosity model), yielding to *mixed-Smagorinsky* or *mixed-σ* models.

2.3 Dynamic procedures

All the four LES models described above (Smagorinsky, σ, mixed-Smagorinsky, and mixed-σ) are characterized by the choice of a suitable constant C. In this work, we used the *dynamic procedure* introduced in [17, 18, 27], based on a second filter (known as *test filter*, indicated in what follows by $\widetilde{\ }$) to be applied to the filtered equations (4). Thus, from the filtered momentum equation $(4)_1$, we obtain

$$\frac{\partial\widetilde{\overline{\boldsymbol{u}}}}{\partial t} - \nu\nabla\cdot\boldsymbol{S}\left(\widetilde{\overline{\boldsymbol{u}}}\right) + \nabla\cdot\left(\widetilde{\overline{\boldsymbol{u}}}\otimes\widetilde{\overline{\boldsymbol{u}}}\right) + \nabla\widetilde{\overline{P}} + \nabla\cdot\widetilde{\boldsymbol{\tau}}^d + \nabla\cdot\boldsymbol{N}^d = \boldsymbol{0} \quad t\in(0,T],\, \boldsymbol{x}\in\Omega, \tag{8}$$

where $\boldsymbol{N}^d$ is the deviatoric part of the *resolved stress* tensor $\boldsymbol{N}$ defined by

$$\boldsymbol{N} = \widetilde{\overline{\boldsymbol{u}} \otimes \overline{\boldsymbol{u}}} - \widetilde{\overline{\boldsymbol{u}}} \otimes \widetilde{\overline{\boldsymbol{u}}}. \tag{9}$$

Alternatively, one could apply the test filter directly to the non-filtered momentum equation $(1)_1$. Supposing that this operation is equivalent to apply successively the grid filter and the test filter (this property is strictly true only when a low-pass filter is employed), we obtain

$$\frac{\partial \widetilde{\overline{\boldsymbol{u}}}}{\partial t} - \nu \nabla \cdot \boldsymbol{S}\left(\widetilde{\overline{\boldsymbol{u}}}\right) + \nabla \cdot \left(\widetilde{\overline{\boldsymbol{u}}} \otimes \widetilde{\overline{\boldsymbol{u}}}\right) + \nabla \widetilde{\overline{P}}^1 + \nabla \cdot \boldsymbol{T}^d = \boldsymbol{0} \quad t \in (0,T],\, \boldsymbol{x} \in \Omega, \tag{10}$$

where, in analogy with the definition of $\boldsymbol{\tau}$ in (2), $\boldsymbol{T}^d$ is the deviatoric part of the subgrid-scale tensor $\boldsymbol{T}$ defined by

$$\boldsymbol{T} = \widetilde{\boldsymbol{u} \otimes \boldsymbol{u}} - \widetilde{\overline{\boldsymbol{u}}} \otimes \widetilde{\overline{\boldsymbol{u}}}. \tag{11}$$

By a direct comparison of (8) and (10) (or equivalently by comparing (2),(9) and (11)), we obtain the so called *Germano identity*, which is at the base of the dynamic procedures:

$$\boldsymbol{T} - \widetilde{\boldsymbol{\tau}} = \boldsymbol{N}. \tag{12}$$

Thanks to their definitions (2) and (11), both the subgrid-scale tensors $\boldsymbol{\tau}$ and $\boldsymbol{T}$ are not computable in principle, due the presence of the terms $\overline{\boldsymbol{u} \otimes \boldsymbol{u}}$ and $\widetilde{\boldsymbol{u} \otimes \boldsymbol{u}}$ which involve the unfiltered velocity $\boldsymbol{u}$. This is the reason why we needed to model them. On the contrary, thanks to the Germano identity (12) and (9), the difference $\boldsymbol{N}$ between the two subgrid stress tensors $\boldsymbol{T}$ and $\boldsymbol{\tau}$ is known in terms of $\overline{\boldsymbol{u}}$, hence it is in principle computable.

We can rewrite in compact form the modeled subgrid stress tensor (5) of the four LES models introduced above as follows:

$$\boldsymbol{\tau}^d\left(\overline{\boldsymbol{u}}\right) = \alpha \boldsymbol{\mathcal{L}}^d\left(\overline{\boldsymbol{u}}\right) - 2C\overline{\Delta}^2 \beta\left(\overline{\boldsymbol{u}}\right) \boldsymbol{S}\left(\overline{\boldsymbol{u}}\right), \tag{13}$$

where $\alpha = 1$ for the mixed models, $\alpha = 0$ otherwise, and where $\beta = \sqrt{2\sum_{i,j} \overline{S}_{ij}\overline{S}_{ij}}$ for the Smagorinsky models and $\beta = \frac{\sigma_3(\sigma_1-\sigma_2)(\sigma_2-\sigma_3)}{\sigma_2^2}$ for the σ models. Thus, we can think to use the same model also for the subgrid tensor $\boldsymbol{T}$, obtaining

$$\boldsymbol{T}^d\left(\widetilde{\overline{\boldsymbol{u}}}\right) = \alpha \boldsymbol{L}^d\left(\widetilde{\overline{\boldsymbol{u}}}\right) - 2C\widetilde{\Delta}^2 \beta\left(\widetilde{\overline{\boldsymbol{u}}}\right) \boldsymbol{S}\left(\widetilde{\overline{\boldsymbol{u}}}\right), \tag{14}$$

where $\widetilde{\Delta}$ is the characteristic length of the test filter, $\boldsymbol{L}^d$ is the deviatoric part of $\boldsymbol{L}$, which, in analogy with the definition of $\boldsymbol{\mathcal{L}}$ in (7), is defined by

$$\boldsymbol{L} = \widetilde{\widetilde{\overline{\boldsymbol{u}}} \otimes \widetilde{\overline{\boldsymbol{u}}}} - \widetilde{\widetilde{\overline{\boldsymbol{u}}}} \otimes \widetilde{\widetilde{\overline{\boldsymbol{u}}}},$$

[1]Notice that here and in the previous NS momentum equation, P has been modified in order to include the terms $\frac{1}{3}\sum_k N_{kk}$ and $\frac{1}{3}\sum_k T_{kk}$, respectively.

and where we have assumed that the constant C is the same used for modeling $\boldsymbol{\tau}^d$ (see, e.g., [18]). Now, by using the Germano identity (12) for the deviatoric part of $\boldsymbol{N}$ in combination with (13) and (14), we obtain

$$\boldsymbol{N}^d = \alpha \left(\boldsymbol{L}^d - \widetilde{\boldsymbol{\mathcal{L}}}^d \right) + C\boldsymbol{M}, \tag{15}$$

where we have set $\boldsymbol{M} = 2\left(\overline{\Delta}\beta\widetilde{\boldsymbol{S}\left(\overline{\boldsymbol{u}}\right)} - \widetilde{\Delta}\beta\boldsymbol{S}\left(\widetilde{\overline{\boldsymbol{u}}}\right)\right)$. The tensors $\boldsymbol{N}^d, \boldsymbol{L}^d, \widetilde{\boldsymbol{\mathcal{L}}}^d$ and $\boldsymbol{M}$ are all computable, since they depend on $\overline{\boldsymbol{u}}$, so that (15) provides a way to compute the constant C. Since the latter cannot be chosen to match the five independent components of the tensors appearing in (15), a least-square minimization has been proposed by [27], obtaining the following expression of the constant to be used in our LES models:

$$C(t, \boldsymbol{x}) = \frac{\sum_{i,j} M_{ij} \left(N_{ij}^d - \alpha \left(L_{ij}^d - \widetilde{\mathcal{L}}_{ij}^d \right) \right)}{\sum_{i,j} M_{ij} M_{ij}}, \tag{16}$$

where we have highlighted that C is a function of time and space.

Notice that neither problem (8) nor (10) are explicitly solved, so that most of the computational effort of the dynamic procedure is taken by the solution of the NS problem (4).

3 Numerical discretization

3.1 About the filtering procedures

In this paper, for the grid filter we considered an *implicit* procedure, given by the solution of the fluid equations on a mesh (coarser than the DNS one), which is not able to capture all the scales up to the Kolmogorov one [36]. In this case $\overline{\Delta}$ represents the size of the mesh. This empirical choice was first proposed by Deardorff [12] and is the most widely used today. In our cases, the mesh is given by a finite element triangulation made by tethrahedra and the size of the mesh has been chosen so as to guarantee independence of the results of LES up to a tolerance of 4% in the wall shear stresses, in accordance with the grid convergence test proposed in [8].

The test filter used to obtain the expression of an effective constant C in a dynamic procedure is described in [49]. In particular, this filter is based i) on computing in each tetrahedra the average velocity $\boldsymbol{w}$ of the grid-filtered velocity $\overline{\boldsymbol{u}}$, and ii) on assigning to each node $\boldsymbol{x}_i$ the velocity field $\widetilde{\overline{\boldsymbol{u}}}$ obtained by averaging the values $\boldsymbol{w}$ related to the tetrahedra that share $\boldsymbol{x}_i$. The characteristic length $\widetilde{\Delta}$ related to this geometric filter is equal to the sum of the volumes of the tetrahedra sharing the node $\boldsymbol{x}_i$.

3.2 Time and space discretization

As for the time discretization, we proposed to use a semi-implicit approach to linearize the momentum equation $(4)_1$, used in combination with a BDF2 scheme [21]. In particular, the convective and the eddy-viscosity terms have been treated semi-implicitly, whereas the Bardina term $\boldsymbol{\mathcal{L}}$ and the constant C in the dynamic cases have been treated explicitly. Instead, for the space discretization we used Finite Elements with a SUPG stabilization term added to control numerical instabilities due to the large convective term [46]. In particular, we used $P2-P2$ Finite Elements, that is piecewise quadratic polynomials for the approximation of the pressure and each velocity component.

In summary, the discretized-in-time Galerkin problem at each time step $t^{n+1} = (n+1)\Delta t$ (Δt being the time discretization parameter) is given by:

Find the velocity $\overline{\boldsymbol{u}}^{n+1}$ and the pressure $\overline{P}^{n+1}$ such that it holds true

$$\left(\frac{3\overline{\boldsymbol{u}}^{n+1} - 4\overline{\boldsymbol{u}}^{n} + \overline{\boldsymbol{u}}^{n-1}}{2\Delta t}, \boldsymbol{v}\right) + \nu\left(\boldsymbol{S}(\overline{\boldsymbol{u}}^{n+1}), \nabla \boldsymbol{v}\right) + \left(\nabla \cdot \left(\overline{\boldsymbol{z}}^{n+1} \otimes \overline{\boldsymbol{u}}^{n+1}\right), \boldsymbol{v}\right) - \left(\overline{P}^{n+1}, \nabla \cdot \boldsymbol{v}\right) +$$
$$+ \left(\alpha \boldsymbol{\mathcal{L}}^{d}(\overline{\boldsymbol{z}}^{n+1}) - 2C^{n}\overline{\Delta}^{2}\beta\left(\overline{\boldsymbol{z}}^{n+1}\right)\boldsymbol{S}\left(\overline{\boldsymbol{u}}^{n+1}\right), \nabla \boldsymbol{v}\right) + M\left(\overline{\boldsymbol{u}}^{n+1}, \overline{P}^{n+1}, \boldsymbol{v}\right) = F(\boldsymbol{v}) \quad \forall \boldsymbol{v} \in \boldsymbol{V}_h,$$
$$(q, \nabla \cdot \overline{\boldsymbol{u}}^{n+1}) = 0 \quad \forall q \in Q_h,$$

where $\overline{\boldsymbol{z}}^{n+1} = 2\overline{\boldsymbol{u}}^{n} - \overline{\boldsymbol{u}}^{n-1}$, $C^{n}(\boldsymbol{x}) = C(t^{n}, \boldsymbol{x})$,

$$M(\boldsymbol{w}, q, \boldsymbol{v}) = \gamma \sum_{K \in \mathcal{T}_\Omega} \delta_{SUPG} \left[F(\boldsymbol{v}) - \left(\left(\frac{3\boldsymbol{w} - 4\overline{\boldsymbol{u}}^{n} + \overline{\boldsymbol{u}}^{n-1}}{2\Delta t} - \nabla \cdot \left(\overline{\boldsymbol{z}}^{n+1} \otimes \boldsymbol{w}\right) - \nabla \overline{q} \right), \boldsymbol{v} \right)_{L^2(K)} + \right.$$
$$\left. + \left(\left(\nu \nabla \cdot \boldsymbol{S}(\boldsymbol{w}) - \nabla \cdot \boldsymbol{\tau}^{d}(\boldsymbol{w}) \right), \nabla \boldsymbol{v} \right)_{L^2(K)} \right]$$

accounts for the SUPG stabilization with $\delta_{SUPG} = \left[\left(\frac{2}{\Delta t} \right)^2 + \left(\frac{2 \parallel \overline{\boldsymbol{u}}^{n} \parallel_\infty}{h} \right)^2 + \left(\frac{4\nu}{h^2} \right) \right]^{-1/2}$ and γ a suitable scaling factor [46, 48], F for possible non homogeneous boundary conditions, $\boldsymbol{v}$ are the test functions, $\boldsymbol{V}_h$ and Q_h are the velocity and pressure Finite Element spaces, K is a generic tetrahedra belonging to the finite elements partitioned domain $\mathcal{T}_\Omega$, h is the maximum element diameter and $(\cdot, \cdot)$ denotes the $L^2(\Omega)$ inner product.

4 Numerical results and discussion

4.1 Details of the simulations and boundary conditions

All the numerical results have been obtained using the parallel Finite Element library `LIFEV` developed at MOX - Politecnico di Milano, INRIA - Paris, CMCS - EPF of Lausanne and Emory University - Atlanta. The partitioning of the mesh

relies on `ParMETIS` (http://glaros.dtc.umn.edu/gkhome/views/metis), whereas the solution of the linear system on `Trilinos` (http://trilinos.sandia.gov). In particular, the linear system arising at each time step has been solved with GMRes, preconditioned with an Additive Schwarz preconditioner available in the package `Ifpack` of Trilinos. LES simulations were run on a 5 nodes and 160 Intel E5-4610v2 cores cluster with 256GB memory per node, using from 96 to 128 cores. DNS simulations were run on a 503 nodes and 12049 Intel Westmere-EP cores cluster with 36GB memory per node, using 480 cores.

We considered a real scenario of a human carotid geometry reconstructed by MRI images, see Figure 1, left. At the Common Carotid Artery (CCA), Γ_{CCA},

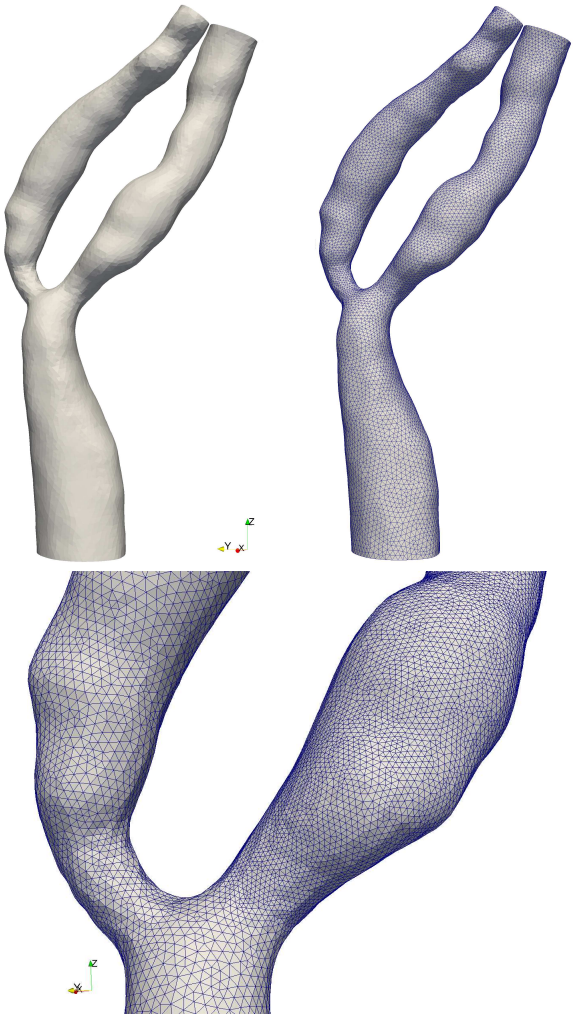

Figure 1: Reconstructed geometry (left), mesh used for the LES computations (center), and DNS refinement at ICA (right).

we imposed the following boundary measure of the flow rate $Q_{CCA}(t)$ obtained

with Echo-Color Doppler and reported in Figure 2

$$\int_{\Gamma_{CCA}} \overline{\boldsymbol{u}} \cdot \boldsymbol{n}\, d\sigma = Q_{CCA}.$$

This is a defective boundary condition, since at each time step we are prescribing only a scalar quantity over Γ_{CCA} rather than 3 conditions for each point of the section. In order to fill this gap, we made the assumption of parabolic velocity profile along the normal direction (suitable choice for carotids [6]), yielding the following Dirichlet boundary condition

$$\boldsymbol{u} = \boldsymbol{g}_{CCA} \qquad t \in (0,T],\, \boldsymbol{x} \in \Gamma_{CCA}.$$

Here $\boldsymbol{g}_{CCA}$ is the unique function characterized by a parabolic profile in the normal direction and vanishing in the tangential ones, whose flow rate at each time step equals $Q_{CCA}(t)$.

In absence of patient-specific measures of the flow rate at the outlets, we have assumed a flow division in the two branches. Indeed, they carry the blood in different regions of the head, namely ICA supplies the brain, whereas ECA the cheeks, and thus they encounter different downstream resistances. Since the estimation of such resistances for the patient at hand would require measurements that we do not have, we fix their values by imposing a fixed-in-time flow division. Specifically, we have prescribed an amount of 65% of the CCA flow rate at the Internal Carotid Artery (ICA) outlet, Γ_{ICA}, [24]

$$\int_{\Gamma_{ICA}} \overline{\boldsymbol{u}} \cdot \boldsymbol{n}\, d\sigma = 0.65 \cdot Q_{CCA}.$$

In this case, the prescription of a selected velocity profile (flat or parabolic) lead to unstable results, since the swirling blood flow generated after the stenosis barely fitted the selected profile at the ICA. For this reason, we have prescribed the flow rate by means of the *augmented formulation*, based on the introduction of a Lagrange multiplier [14, 50]. In fact, this leads to the prescription of the following Neumann condition

$$-\overline{P}\boldsymbol{n} + \nu \boldsymbol{S}(\overline{\boldsymbol{u}})\boldsymbol{n} - \boldsymbol{\tau}^d(\overline{\boldsymbol{u}})\boldsymbol{n} = \lambda \boldsymbol{n} \qquad t \in (0,T],\, \boldsymbol{x} \in \Gamma_{ICA},$$

where $\lambda(t)$ is the unknown Lagrange multiplier. This strategy has been shown to be effective in real applications, see, e.g. [35] for the case of abdominal aortic aneurysms and [52, 51] for the ascending aorta. Due to the rigid wall assumption we have made in this work [34], at the External Carotid Artery (ECA), Γ_{ECA}, in accordance with the incompressibility constraint, we prescribed the homogeneous Neumann condition

$$-\overline{P}\boldsymbol{n} + \nu \boldsymbol{S}(\overline{\boldsymbol{u}})\boldsymbol{n} - \boldsymbol{\tau}^d(\overline{\boldsymbol{u}})\boldsymbol{n} = \boldsymbol{0} \qquad t \in (0,T],\, \boldsymbol{x} \in \Gamma_{ECA}.$$

This guarantees that the physiological value of 35% of the CCA flow rate is coming in the ECA. For each case we run the simulation over four cardiac cycles.

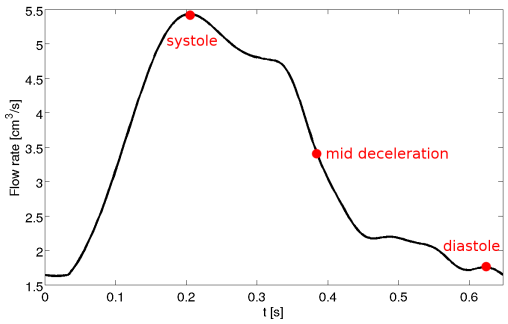

Figure 2: Flow waveform used for inlet boundary condition (CCA) based on Echo-Color Doppler in vivo measurements.

We neglected however the first one, so that all the reported results refer to three cycles.

The mesh for LES computations was formed by $4.12 \cdot 10^5$ tetrahedra, see Figure 1, center. For the DNS we used a mesh obtained by a refining strategy in the regions where turbulence effect have been expected (that is at the bifurcation and ICA) composed by 10^6 tetrahedra (see Figure 1, right). We used also the following data: physical viscosity $\nu = 0.033\, dyne/cm^2$, fluid density $\rho_f = 1.06\, g/cm^3$, time discretization parameter $\Delta t = 6.25 \cdot 10^{-4}\, s$, period of one heart beat $T = 0.6475s$, scaling factor in the SUPG $\gamma = 0.01$.

To avoid numerical instabilities it is customary to limit the SGS stress tensor contribution. We imposed that the total viscosity is positive and, to avoid too large values, bounded, in particular we set $-\nu \leq \nu_{sgs} \leq 10\nu$.

To quantify the variation of a physical quantity $S(t, \boldsymbol{x})$ over the cardiac cycles and thus to highlight the related turbulent effects, we compute the *ensemble-averages* $\mathcal{S}(\boldsymbol{x})$ of S at the systolic and mid-deceleration points along the cardiac cycles, as follows:

$$\mathcal{S}(\boldsymbol{x}) = \frac{1}{M} \sum_{j=1}^{M} S(t_i + (j-1)T), \;\; i = s, md,$$

where $M = 3$ is the number of cardiac cycles.

As for the choice of the mesh size and of the Δt in the DNS simulation, we refer the reader to the next subsection.

4.2 On the choice of the discretization parameters

In our case, due to the complex geometry and pulsatile forcing terms, transitional effects downstream the stenosis are present, so that the classical Kolmogorov theory that predicts the size of the smallest scales of statistically homogeneous isotropic and stationary turbulence may be insufficient. Therefore, we used an alternative approach to define our DNS mesh size and time step. As observed,

at the systole long shear layers are created and their instability can trigger the transition to turbulence during the deceleration phase. Thus, we labelled the mesh "fine" when it was able to correctly resolve the shear layers detaching from the stenosis in the ICA, since this is the primary phenomenon characterizing the blood flow in stenotic carotids [23]. The same holds for the choice of the time discretization parameter Δt.

To this aim, we considered the simplified problem of a viscous, incompressible, and two-dimensional laminar shear layer [4], characterized by the following velocity field

$$\boldsymbol{u}(x,y) = \begin{pmatrix} U_{shear}\tanh(y/L_{shear}) \\ 0 \end{pmatrix},$$

for a suitable constant U_{shear} and where L_{shear} is the shear layer width. Then, we apply a perturbation of the form

$$\boldsymbol{u}^P(t,x,y) = \begin{pmatrix} i\alpha\frac{dv}{dy} \\ v(y)e^{i\alpha x - i\omega t)} \end{pmatrix},$$

to the two-dimensional laminar shear layer, where, given $\alpha \in \mathbb{R}$, the eigenfunction v and the corresponding eigenvalue $\omega = \omega_r + i\omega_i \in \mathbb{C}$ are determined by the *Orr-Sommerfeld* equation obtained by linearizing the Navier-Stokes equations [39]. In [4] it has been shown that the most unstable eigenvalues have null real part ($\omega_r \simeq 0$), so that the associated modes are characterized by an exponential growth in time. Given a Reynolds number, by plotting the largest value of $\omega_i = \omega_i(\alpha)$ as a function of α we obtain a curve from which we derived the maximum value of ω_i, $\omega_{i,max}$, and the maximum value of α, α_{max}, such that $\omega_i(\alpha) > 0$ for each $\alpha \leq \alpha_{max}$. In this work, we propose to choose the discretization parameters h and Δt so as to guarantee that $h^{crit} = A/\alpha_{max}$ and $\Delta^{crit}t = B/\omega_{i,max}$, where $A, B \leq 1$ are constants chosen to ensure accuracy.

In order to compute the Reynolds number of the shear layers in our carotid simulation, we considered a simulation without any LES model with values of the space and time discretization parameters h^{Re} and Δt^{Re} which guaranteed the independence of the wall shear stresses (up to a tolerance of 4%) obtaining

$$Re_{shear} = \frac{U_{shear}L_{shear}}{\nu} = 7.6.$$

In our case $L_{shear} = 0.01\,cm$ is the shear layer thickness at the stenosis and $U_{shear} = 25\,cm/s$ is the velocity in the shear layer center. We found (see figure 3) the following values of the discretization parameters which allow to resolve the most unstable wave associated with the Kelvin-Helmhotz instability:

$$h^{crit} = 0.028\,cm, \qquad \Delta t^{crit} = 6.25 \cdot 10^{-4}\,s,$$

where we have used $A = 0.2$ and $B = 0.1$. We observe that the values of h^{Re} and Δt^{Re} used to estimate the Reynolds numbers are coherent with the estimates h^{crit} and Δt^{crit}.

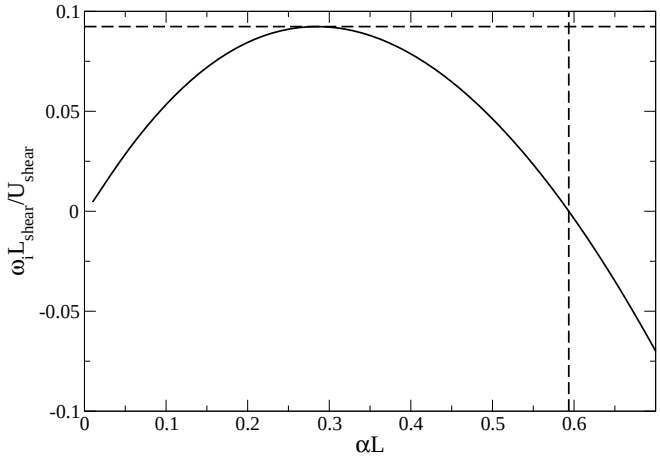

Figure 3: Growth rate for the shear layer instabilities at Reynolds number $Re_{shear} = 7.6$ as a function of the normalized spatial frequency αL_{shear} [4]. The two dashed lines mark the maximum normalized spatial frequency characterized by positive values of ω_i (corresponding to an unstable shear layer, $\alpha_{max} L_{shear} \simeq 0.594$) and the maximum growth rate ($\omega_i L_{shear}/U_{shear} \simeq 0.0924$).

4.3 Results and discussion

4.3.1 Description of the DNS solution

Our first analysis concerns the description of the shear layers dynamics found by our DNS simulation. We considered three time instants in the cardiac cycle, namely the systolic peak t_s, a mid-deceleration point t_{md}, and a diastolic point, see Figure 2. We observe that all the numerical results related to the diastolic point featured a laminar behavior, so that we do not report them in what follows. Rather, we will focus only on the ICA, since the flow remains laminar in the CCA and in the ECA through the whole cardiac cycle and for this reason it is not reported here.

First of all we studied the dependence of the DNS solution on the choice of Δt. In Figure 4 we report the mean time energy spectra over three cardiac beats at location (a) as a function of the Strouhal number $St = \omega\, D/U_{mean}$ obtained with the value of Δt predicted by the 2D analysis of previous subsection and with a value four times greater. In our case $D = 0.2\, cm$ is the stenosis diameter and $U_{mean} = 80\, cm/s$ is the average-in-time and in-space velocity. From these results we observe the significant differences between the two spectra. In particular, the largest value of Δt is not able to identify the peak frequency characterizing the shear layers dynamics and overestimates the energy at the medium and high frequencies. We remark that the peak observed for $St = 1.05$ corresponds to $\omega = (St\, U_{mean})/D \simeq 400\, Hz$ which is of the same order of magnitude of the growth rate deduced from Figure 3 $\omega_{i,max} \simeq 0.0924 \cdot U_{shear}/L_{shear} = 250\, Hz$. This test on the sensitivity of the solution on Δt highlights the importance of

the choice of the time discretization parameter in performing a DNS. We did not experience any significant difference among the numerical solutions when Δt smaller than Δt^{crit} were used. Thus, from now on, all the results that we present are obtained by using $\Delta t = \Delta t^{crit} = 6.25 \cdot 10^{-4}\, s$.

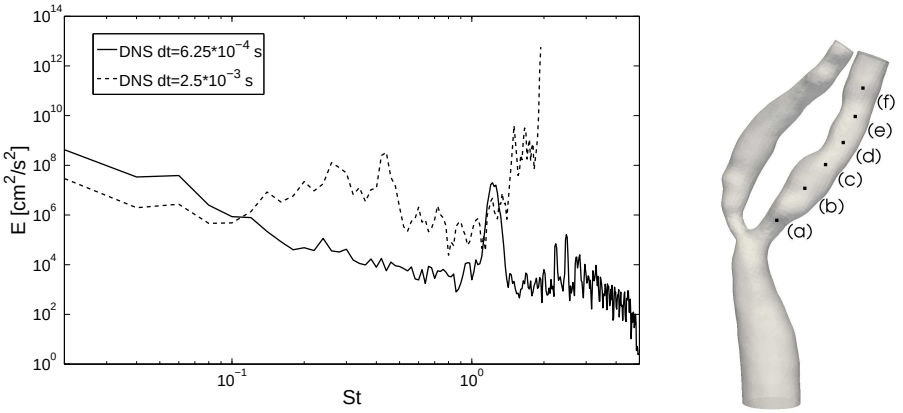

Figure 4: Mean time energy spectra at location (a) for DNS with different values of Δt.

In Figure 5, top, we report the ensemble-averaged velocity field at six time frames around the systole. We observe, as expected, the formation of two shear layers at both sides of the jet. These shear layers, which are compact and intact at the beginning of the sequence, start to oscillate just below the wall impingement region and, after about $0.05\, s$, the jet inside the shear layers breaks down leading to chaotic and random swirling structures downstream. In particular, we observe that transitional effects appear in the DNS after approximatively three stenosis diameters from the bifurcation.

In Figure 6 we report the ensemble-averaged vorticity $\mathcal{W}$ at the systolic and mid-decelaration points, at a longitudinal section of the ICA. From the DNS results, we observe that the flow is transitional in the ICA at both the systolic and the mid-deceleration phases. Indeed, the behavior of the vorticity $\mathcal{W}$ at the systole highlights a non-compact impingement of the flow jet, which features a waving motion before reaching the ICA wall and clearly shows the presence of the two unstable shear layers. At the mid-deceleration point, the instabilities are still well highlighted by the vorticity $\mathcal{W}$.

4.3.2 Comparison between LES and DNS

The aim of this section is to provide a comparison among the solutions obtained by DNS and the LES models described above (dynamic and dynamic mixed-Smagorinsky, static and dynamic σ, dynamic mixed-σ).

We found numerical instabilities during the deceleration phase after systole using the dynamic Smagorinsky and the dynamic mixed-Smagorinsky models,

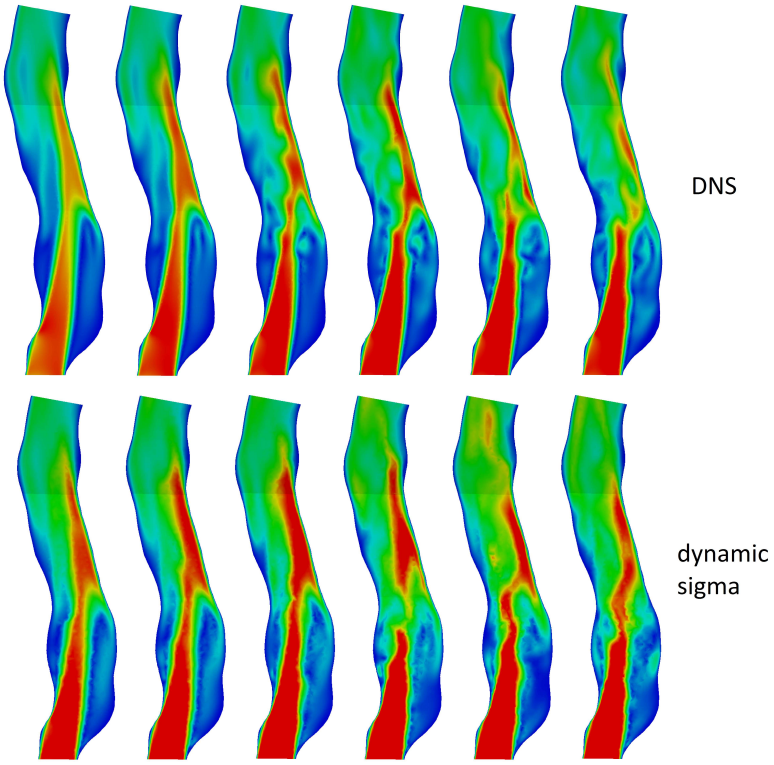

Figure 5: Ensemble-averaged velocity magnitude for DNS (top) and dynamic σ model (bottom) at six temporal frames spaced out one from the other by $0.02\,s$. The fourth frame corresponds to the systolic peak.

which lead to the interruption of these simulations. The instabilities are probably due to the fact that the function C in (16) is highly intermittent in space and time. We could not average it, as is commonly done in situations with statistically spatial homogeneity directions or temporal stationarity [18, 54], due to the very different physical regimes that are present in our system both in space and time. Instead, the static σ, the dynamic σ and the dynamic mixed-σ models turned out to be robust and were less affected by the intermittence of C, so that in what follows we analyze only the results of these models. In the following figures, we refer to them as "sigma","dyn-sigma" and "dyn-m-sigma".

In Figure 7, top, we report the velocity magnitude for three cycles at six different centerline locations along the ICA, for DNS and static σ model. These results highlight that just after the stenosis (location (a)) the flow is still in a laminar regime. Instead, downstream the stenosis (locations (b)-(f)) complex velocity oscillations occur. We notice that oscillations featured by the static σ model appear and disappear at the same time instants with respect to the DNS, whereas for the dynamic models oscillations occur on a wider temporal range (see zooms reported in Figure 7, bottom). We also observe that at location (b)

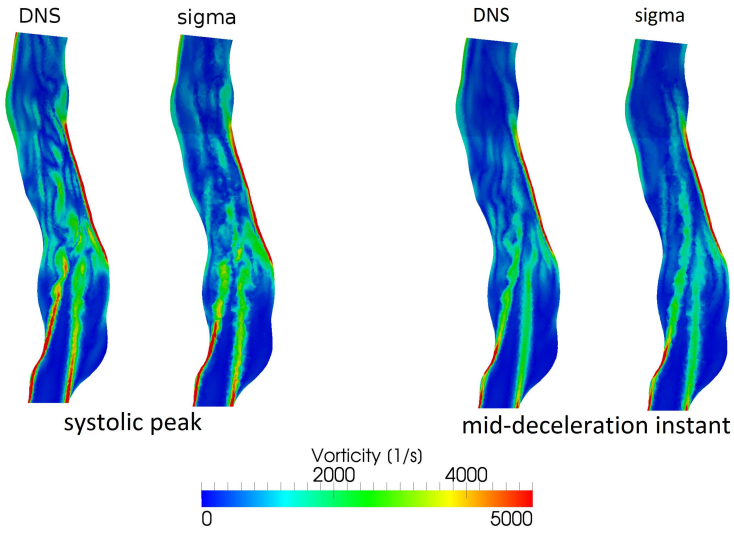

Figure 6: Ensemble-averaged vorticity at the systolic point t_s (left) and at the mid-deceleration point t_{md} (right). For each instant, DNS at the left and static σ at the right.

the values of the velocity obtained by the static σ model are larger than the DNS ones during the first part of the systolic phase. On the contrary, the dynamic σ model overpredicts the velocity magnitude at the end of the systolic phase. The dynamic mixed-σ model produces larger values during the whole systolic phase. We finally notice that at location (b) both dynamic models feature higher large frequency oscillations with respect to DNS and static model. Downstream (locations (c)-(f)), the behavior of all the LES models is in excellent agreement with DNS. Due to the comparable results among the three LES models at these four locations, we reported in Figure 7, top, only the static case. The overproduction of energy by the mixed model in the shear layers observed at location (b) is counter-balanced by its overdissipation in the downstream locations. The overdissipation of mixed models in developed turbulence is often reported, see e.g. [54].

In Figure 8 we reported the time energy spectra of the velocity magnitude as a function of the Strouhal number for DNS and static σ model at three of the locations depicted in Figure 7. We observe from the energy spectra of location (a) that the energy behavior obtained by the static model is almost coincident with the DNS one. This is not surprising since at this location we are in laminar regime. Also at the downstream locations (where the transitional effects are relevant) we can observe an excellent agreement between the static model and DNS.

This is not the case of the dynamic models. For example, in the same figure at the bottom we reported the velocity magnitude at location (a) for the dynamic

σ model and the corresponding energy spectrum (the latter also for the dynamic mixed model). These results highlight small spurious high frequency oscillations for the velocity magnitude which are clearly visible in the related spectrum. A similar trend has been observed for the velocity obtained by the dynamic mixed model, not reported here. In Figure 8 we also reported the energy spectra of dynamic models at location (b). We notice that both models (especially the mixed one) overestimate the energy both at low and high frequencies. This confirms the previous observation about Figure 7, bottom, which highlighted stronger large frequencies oscillations for the dynamic models. This increased energy at medium and high frequencies at location (b) is probably a remnant of the overestimated energy generated upstream which, due to the dissipation, is less marked than at the previous location (a). At locations (c)-(f), where disturbed and chaotic structures developed, the energy spectra of the dynamic models fit well the DNS ones, confirming the accuracy of these models at the downstream locations. In particular, there are no more differences among the spectra at the medium and high frequencies. For this reason, we did not report these spectra. The increased oscillations featured by the dynamic models at the upstream locations, that is at the beginning of the transition, could be due to the dynamic computation of the coefficient C which is very variable function of space and time. This can destabilize the solution, as already seen for the Smagorinky model where this effect was such evident to destroy the numerical stability. To the aim of seeking a more stable and accurate numerical solution, we investigated the results obtained by considering at each time step a global value of C in the dynamic procedures obtained by averaging in space the local constants. However, the results showed a very dissipative solution which was not able at all to represent accurately the shear layers dynamics, so that we do not report them.

To better describe the behaviour of the dynamic σ model, in Figure 5, bottom, we reported the ensemble-averaged velocity field at the same six time frames considered for DNS (see Figure 5, top). From these results, we observe that oscillations and breakage of the jet and shear layers start for the dynamic model earlier than DNS. This is in agreement with the velocity oscillations observed in Figure 7, bottom, which for the dynamic model start before the systolic peak, unlike DNS.

The good behaviour of the results obtained by the static σ model is also confirmed by looking at the ensemble-averaged vorticity $\mathcal{W}$ at a longitudinal section of the ICA reported in Figure 6 at the systolic and mid-decelaration instants. From these results, we observe that the static model is in excellent agreement with DNS.

In Figure 9 we report the in-plane ensemble-averaged velocity fields at the systole for several cross sections. In particular, the velocity pattern at the more proximal location A-A is very similar for all the four cases considered, whereas at location B-B and C-C the static model features a better agreement with the DNS with respect to the dynamic models, confirming what found previously.

However, for the distal locations D-D, E-E and F-F, the accuracy of the dynamic models is very good (confirming again what found previously), even better than the static one.

Finally, we observe that for stenotic carotids a major clinical role is played by the Wall Shear Stresses (WSS). Indeed, high systolic WSS could promote the plaque rupture [20] and a hammer effect at the ICA wall [26]. Thus, a natural question arising from the clinical point of view is whether the accuracy of LES models are able to predict correct values of WSS. To answer this question, in Figure 10 we report the systolic WSS for DNS and the three σ models. We observe again the excellent agreement of the results obtained by the static model with DNS and the overall very good beahavior of the dynamic ones.

5 Conclusions

In this work we have considered for the first time Large Eddy Simulations (LES) models to describe the transitional effects appearing in real vascular districts, in particular in stenotic carotids. The main contributions and outcomes of the present work are summarized in what follows:

1. We proposed a way based on a simplified 2D shear layer model to estimate the grid size and time discretization parameter needed to capture all the important features of the fluid flow in a stenotic carotid, in particular the dynamics of the jet and of the shear layers. We referred to this simulation as DNS;

2. The shear layers generated after the bifurcation are well captured by the static σ model. The shear layers obtained by the dynamic and dynamic mixed- models are less stable than the DNS ones and consequently they break up earlier in space and time;

3. The velocity fluctuations and the time energy spectra are well described by the static σ model at each locations along the ICA, and by the dynamic models sufficiently far from the bifurcation (locations (c)-(f));

4. Among the dynamic models, dynamic σ is more accurate than mixed-σ in terms of similarity of the velocity field with the DNS one;

5. All the σ models were able to capture the peak oscillation frequency of the shear layers.

The next steps will be the applications to different arterial districts (such as the aorta), the inclusion of fluid-structure interaction to account for the vessel displacements, and the test of turbulence models that take into account anisotropy effects [1].

Acknowledgments

All the simulations run on a cluster at MOX Dipartimento di Matematica, Politecnico di Milano, Italy, and on the Certainty cluster at the Center for Turbulence Research, Stanford University, Stanford (CA), USA. RML was partially supported by the GNCS - INdAM funding n. U 2014/000542. He is grateful to Prof. Gianluca Iaccarino for his availability and his fruitful suggestions. CV and AQ has been partially supported by the Italian MIUR PRIN09 project no. 2009Y4RC3B 001. The research of AQ was also supported by the Swiss National Science Foundation (SNF), project no. 140184.

References

[1] A. Abbà, C. Cercignani, and L. Valdettaro. Analysis of subgrid scale models. *Computers and Mathematics with applications*, 46:521–535, 2003.

[2] S.A. Ahmed and D.P. Giddens. Pulsatile poststenotic flow studies with laser Doppler anemometry. *J Biomech*, 17(9):695–705, 1984.

[3] J. Bardina, J.H. Ferziger, and W.C. Reynolds. Improved turbulence models based on LES of homogeneous incompressible turbulent flows. *Report No. TF-19, Department of Mechanical Engineering, Stanford*, 1984.

[4] R. Betchov and A. Szewczyk. Stability of a shear layer between parallel streams. *Physics of Fluids*, 6(10):1391–1396, 1963.

[5] D. Birchall, A. Zaman, J. Hacker, G. Davies, and D. Mendelow. Analysis of haemodynamic disturbance in the atherosclerotic carotid artery using computational fluid dynamics. *European Radiology*, 16(5):1074–1083, 2006.

[6] I.C. Campbell, J. Ries, S.S. Dhawan, A.A. Quyyumi, W.R. Taylor, and J.N. Oshinski. Effect of inlet velocity profiles on patient-specific computational fluid dynamics simulations of the carotid bifurcation. *J Biomech Eng*, 134(5):051001, 2012.

[7] R.A. Cassanova and D.P. Giddens. Disorder distal to modeled stenoses in steady and pulsatile flow. *J Biomech*, 11(10-12):441–453, 1978.

[8] I.B. Celik, U. Ghia, P.J. Roache, C.J. Freitas, H. Coleman, and P.E. Raad. Procedure for estimation and reporting of uncertainty due to discretization in CFD applications. *J Fluids Eng Trans ASME*, 130:1–4, 2008.

[9] Tomás Chacón Rebollo and Roger Lewandowski. *Mathematical and Numerical Foundations of Turbulence Models and Applications*. Birkhauser, 2014.

[10] C. Chnafa, S. Mendez, and F. Nicoud. Image-based large-eddy simulation in a realistic left heart. *Computers & Fluids*, 94:173–178, 2014.

[11] C. Clark. The propagation of turbulence produced by a stenosis. *J Biomech*, 13:591–604, 1980.

[12] J.W. Deardorff. A numerical study of three-dimensional turbulent channel flow at large Reynolds numbers. *Journal of Fluid Mechanics*, 41:453–465, 1970.

[13] N. DePaola, M.A. Gimbrone Jr, P.F. Davies, and C.F. Dewey Jr. Vascular endothelium responds to fluid shear stress gradients. *Arteriosclerosis, Thrombosis, and Vascular Biology*, 12:1254–1257, 1992.

[14] L. Formaggia, J.-F. Gerbeau, F. Nobile, and A. Quarteroni. Numerical treatment of defective boundary conditions for the Navier-Stokes equation. *SIAM Journal on Numerical Analysis*, 40(1):376–401, 2002.

[15] L. Formaggia, A. Quarteroni, and A. Veneziani (Eds.). *Cardiovascular Mathematics - Modeling and simulation of the circulatory system*. Springer, 2009.

[16] R. Gardhagen, J. Lantz, F. Carlsson, and M. Karlsson. Quantifying Turbulent Wall Shear Stress in a Stenosed Pipe Using Large Eddy Simulation. *J Biomech Eng*, 132(6):061002, 2010.

[17] M. Germano. Turbulence: the filtering approach. *Journal of Fluid Mechanics*, 238:325–336, 1992.

[18] M. Germano, U. Piomelli, P. Moin, and W.H. Cabot. A dynamic subgrid-scale eddy viscosity model . *Physics of Fluids A*, 3(7):1760–1765, 1991.

[19] L. Grinberg, A. Yakhot, and G.E. Karniadakis. Analyzing Transient Turbulence in a Stenosed Carotid Artery by Proper Orthogonal Decomposition . *Annals of Biomedical Engineering*, 37(11):2200–2217, 2009.

[20] H.C. Groen, F.J. Gijsen, A. van der Lugt, M.S. Ferguson, T.S. Hatsukami, A.F. van der Steen, C. Yuan, and J.J. Wentzel. Plaque rupture in the carotid artery is localized at the high shear stress region: a case report. *Stroke*, 38(8):2379–2381, 2007.

[21] E. Hairer, S.P. Nørsett, and G. Wanner. *Solving ordinary differential equations: Nonstiff problems*. Springer Series in Comput. Math. Springer, 1993.

[22] S. Kefayati, D.W. Holdsworth, and T.L. Poepping. Turbulence intensity measurements using particle image velocimetry in diseased carotid artery models: Effect of stenosis severity, plaque eccentricity, and ulceration. *Journal of Biomechanics*, 47:253–263, 2014.

[23] S.E. Lee, S.W. Lee, P.F. Fischer, H.S. Bassiouny, and F. Loth. Direct numerical simulation of transitional flow in a stenosed carotid bifurcation. *J Biomech*, 41(11):2551–2561, 2008.

[24] S.W. Lee, L. Antiga, J.D. Spence, and D.A. Steinman. Geometry of the carotid bifurcation predicts its exposure to disturbed flow. *Stroke*, 39:2341–2347, 2008.

[25] Z.Y. Li and J.H. Gillard. Plaque rupture: plaque stress, shear stress, and pressure drop. *Journal of the American College of Cardiology*, 52(13):1106–1107, 2008.

[26] D. Liepsch. An introduction to biofluid mechanics - basic models and applications. *Journal of Biomechanics*, 35:415435, 2002.

[27] D.K. Lilly. A proposed modification of the Germano subgridscale closure method . *Physics of Fluids A*, 4(3):633–635, 1992.

[28] S. Liu, C. Meneveau, and J. Katz. On the properties of similarity subgrid-scale models as deduced from measurements in a turbulent jet. *Journal of Fluid Mechanics*, 275:83–119, 1994.

[29] H.M. Loree, R.D. Kamm, C.M. Atkinson, and R.T. Lee. Turbulent pressure fluctuations on surface of model vascular stenoses. *American Journal of Physiology - Heart and Circulatory Physiology*, 261(3):H644–H650, 1991.

[30] M.M. Molla and M.C. Paul. LES of non-Newtonian physiological blood flow in a model of arterial stenosis. *Medical Engineering & Physics*, 34:1079–1087, 2012.

[31] F. Nicoud, H. Baya Toda, O. Cabrit, S. Bose, and J. Lee. Using singular values to build a subgrid-scale model for large eddy simulations. *Physics of Fluids*, 23(8):085106, 2011.

[32] M. Ojha. Wall shear stress temporal gradient and anastomotic intimal hyperplasia. *Circulation Research*, 74:1227–1231, 1994.

[33] M.C. Paul and M.M. Molla. Investigation of physiological pulsatile flow in a model arterial stenosis using large-eddy and direct numerical simulations. *Applied Mathematical Modelling*, 36:4393–4413, 2012.

[34] K. Perktold and G. Rappitsch. Computer simulation of local blood flow and vessel mechanics in a compliant carotid artery bifurcation model. *Journal of Biomechanics*, 28(7):845–856, 1995.

[35] M. Piccinelli, C. Vergara, L. Antiga, L. Forzenigo, P. Biondetti, and M. Domanin. Impact of hemodynamics on lumen boundary displacements in abdominal aortic aneurysms by means of dynamic computed tomography and

computational fluid dynamics. *Biomech Model Mechanobiol*, 12(6):1263–1276, 2013.

[36] S.B. Pope. *Turbulent flows*. Cambridge University Press, 2000.

[37] R.S. Rogallo and P. Moin. Numerical Simulation of Turbulent Flows. *Annual Review of Fluid Mechanics*, 16:99–137, 1984.

[38] M.V. Salvetti and S. Banerjee. A priori tests of a new dynamic subgrid-scale model for finite-difference large eddy simulations. *Phys. Fluids*, 7:2831–2847, 1995.

[39] H. Schlichting. *Boundary Layer Theory*. McGraw-Hill Book Company, Inc., New York, 1963.

[40] C.J. Slager, J.J. Wentzel, F.J. Gijsen, A. Thury, A.C. van der Wal, J.A. Schaar, and P.W. Serruys. The role of shear stress in the destabilization of vulnerable plaques and related therapeutic implications. *Nature Clinical Practice Cardiovascular Medicine*, 2(9):456–464, 2005.

[41] J. Smagorinsky. General circulation experiments with the primitive equations: I. The basic experiment. *Monthly weather review*, 91:99–164, 1963.

[42] W.E. Stehbens. Turbulence of blood flow. *Experimental Physiology*, 44(1):110–117, 1959.

[43] J.S. Stroud, S.A. Berger, and D. Saloner. Numerical Analysis of Flow Through a Severely Stenotic Carotid Artery Bifurcation. *J Biomech Eng*, 124(1):9–20, 2002.

[44] F.P. Tan, G. Soloperto, S. Bashford, N.B. Wood, S. Thom, A. Hughes, and X.Y. Xu. Analysis of Flow Disturbance in a Stenosed Carotid Artery Bifurcation Using Two-Equation Transitional and Turbulence Models. *J Biomech Eng*, 130(6):061008, 2008.

[45] F.P. Tan, N.B. Wood, G. Tabor, and X.Y. Xu. Comparison of LES of Steady Transitional Flow in an Idealized Stenosed Axisymmetric Artery Model With a RANS Transitional Model. *J Biomech Eng*, 133(5):051001, 2011.

[46] T.E. Tezduyar. Stabilized finite element formulations for incompressible flow computations. *Advances in Applied Mathematics*, 28:1–44, 1992.

[47] S.G. Timsit, R.L. Sacco, J.P. Mohr, M.A. Foulkes, T.K. Tatemichi, P.A. Wolf, T.R. Price, and D.B. Hier. Early clinical differentiation of cerebral infarction from severe atherosclerotic stenosis and cardioembolism. *Stroke*, 23(4):486–491, 1992.

[48] L. Tobiska and G. Lube. A modified streamline-diffusion method for solving the stationary Navier-Stokes equations. *Numerische Mathematik*, 59:13–29, 1991.

[49] P. H. Baya Toda. *LES modeling and experimental study of wall-bounded flows in complex geometries*. PhD thesis, Universite Montpellier II, 2011.

[50] A. Veneziani and C. Vergara. Flow rate defective boundary conditions in haemodinamics simulations. *International Journal for Numerical Methods in Fluids*, 47:803–816, 2005.

[51] C. Vergara, F. Viscardi, L. Antiga, and G.B. Luciani. Influence of bicuspid valve geometry on ascending aortic fluid-dynamics: a parametric study. *Artificial Organs*, 36(4):368–378, 2012.

[52] F. Viscardi, C. Vergara, L. Antiga, S. Merelli, A. Veneziani, G. Puppini, G. Faggian, A. Mazzucco, and G.B. Luciani. Comparative finite element model analysis of ascending aortic flow in bicuspid and tricuspid aortic valve. *Artificial organs*, 34(12):1114–20, December 2010.

[53] B. Vreman, B. Geurts, and H. Kuerten. On the formulation of the dynamic mixed subgridscale model. *Physics of Fluids*, 6(12):4057–4059, 1994.

[54] B. Vreman, B. Geurts, and H. Kuerten. Large-eddy simulation of the turbulent mixing layer. *Journal of Fluid Mechanics*, 339:357–390, 1997.

[55] D.M. Wootton and D.N. Ku. Fluid mechanics of vascular systems, diseases, and thrombosis. *Annual Review of Biomedical Engineering*, 1:299–329, 1999.

[56] Y. Zang, R.L. Street, and J.R. Koseff. A dynamic mixed subgridscale model and its application to turbulent recirculating flows. *Physics of Fluids A*, 5(12):3186–3196, 1993.

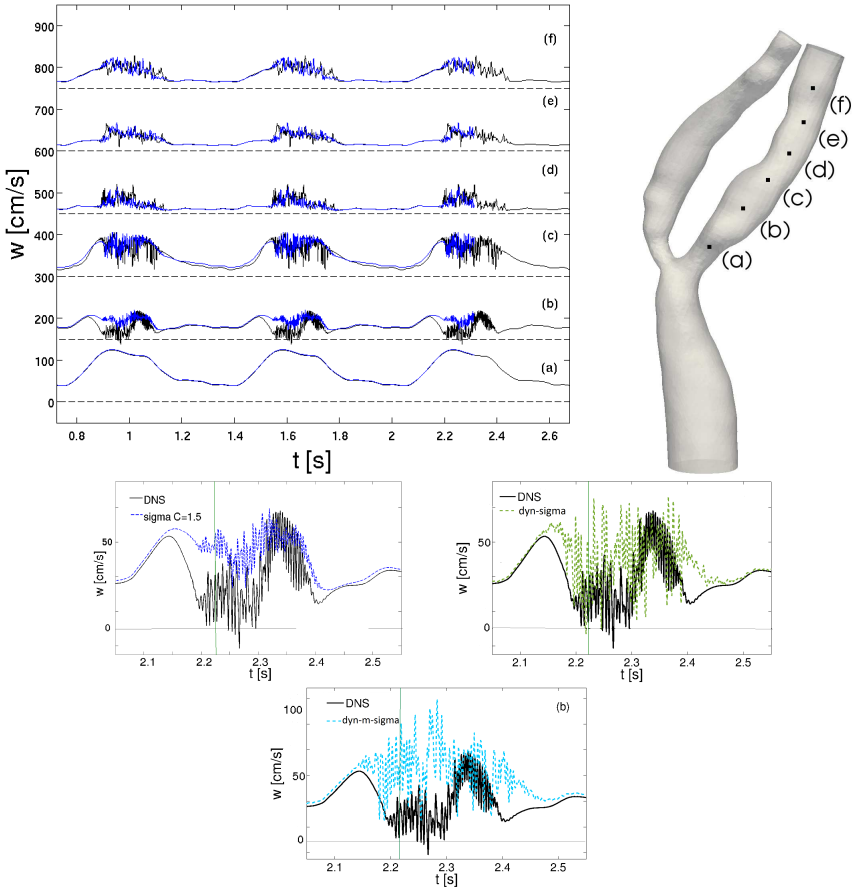

Figure 7: Top view: time traces of the velocity magnitude at six streamwise centerline points for three cardiac cycles for DNS (in black) and static σ model (in blue). An offset in velocity equal to $150\,cm/s$ at each centerline point has been used. Bottom view: particular of the third cycle at location (b) for the static (left), dynamic (middle), and dynamic mixed- (right) σ models. The vertical line represents the systolic peak.

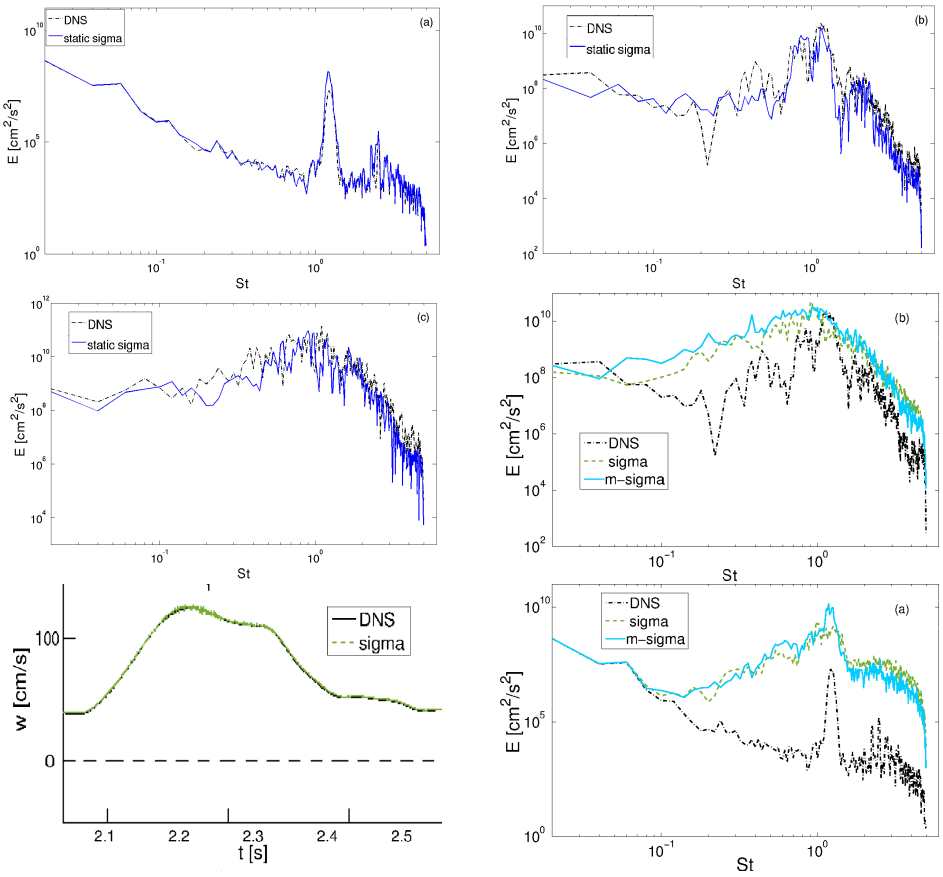

Figure 8: Time energy spectra of the velocity magnitude related to time traces reported in Figure 7. Top, left: static model, location (a); Top, right: static model, location (b); Midlle, left: static model, location (c); Middle, right: dynamic models, location (b); Bottom, right: dynamic models, location (a). At the bottom, left, the velocity magnitude at location (a) for the dynamic model is reported.

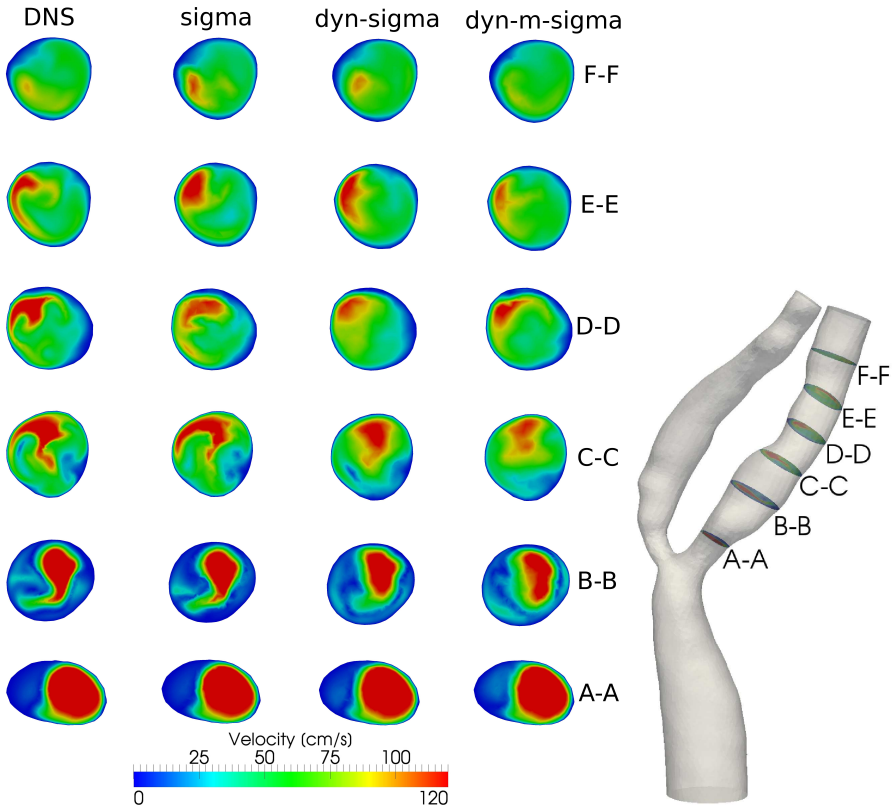

Figure 9: Ensemble-averaged velocity magnitude at six cross-sections along the ICA at the systole. From the left to the right: DNS, static σ, dynamic σ, and dynamic mixed-σ.

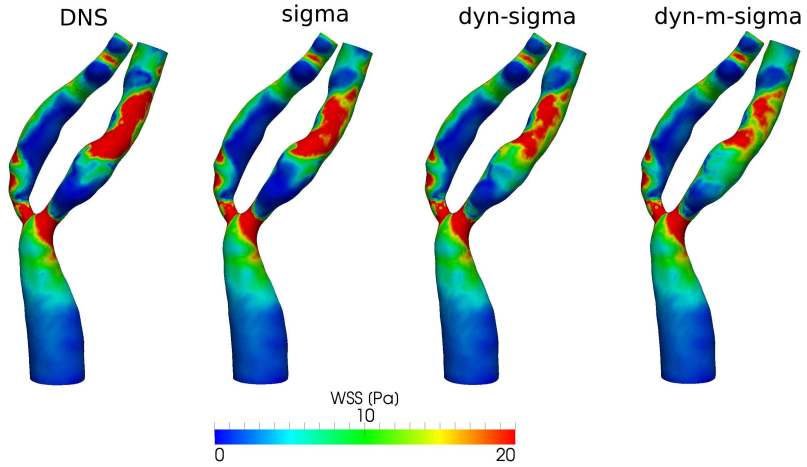

Figure 10: Systolic Wall Shear Stresses for the four models considered.

MOX Technical Reports, last issues

Dipartimento di Matematica
Politecnico di Milano, Via Bonardi 9 - 20133 Milano (Italy)

62/2015 Signorini, M.; Zlotnik, S.; Díez, P.
Proper Generalized Decomposition solution of the parameterized Helmholtz problem: application to inverse geophysical problems.

61/2015 Tagliabue, A.; Dedè, L.; Quarteroni, A.
Fluid dynamics of an idealized left ventricle: the extended Nitsche's method for the treatment of heart valves as mixed time varying boundary conditions

59/2015 Menafoglio, A.; Guadagnini, A.; Secchi, P.
Stochastic Simulation of Soil Particle-Size Curves in Heterogeneous Aquifer Systems through a Bayes space approach

60/2015 Perotto, S.; Reali, A.; Rusconi, P.; Veneziani, A.
HIGAMod: A Hierarchical IsoGeometric Approach for MODel reduction in curved pipes

58/2015 Iapichino, L.; Rozza, G.; Quarteroni, A.
Reduced basis method and domain decomposition for elliptic problems in networks and complex parametrized geometries

57/2015 Wilhelm, M.; Dedè, L.; Sangalli, L.M.; Wilhelm, P.
IGS: an IsoGeometric approach for Smoothing on surfaces

56/2015 Bonaventura, L.; Della Rocca, A.
Monotonicity, positivity and strong stability of the TR-BDF2 method and of its SSP extensions

55/2015 Fumagalli, A.; Zonca, S.; Formaggia, L.
Advances in computation of local problems for a flow-based upscaling in fractured reservoirs

54/2015 Canuto, C.; Nochetto, R. H.; Stevenson, R.; Verani, M.
Adaptive Spectral Galerkin Methods with Dynamic Marking

53/2015 Menafoglio, A; Grujic, O.; Caers, J.
Universal kriging of functional data: trace-variography vs cross-variography? Application to forecasting in unconventional shales